Measurements and Simulations of Athermal Phonon Transmission from Silicon Absorbers to Aluminum Sensors

M. Martinez,[1,2,*] L. Cardani,[3] N. Casali,[3] A. Cruciani,[3] G. Pettinari,[4] and M. Vignati[3]

[1] *Laboratorio de Física Nuclear y Astropartículas, Universidad de Zaragoza, Calle Pedro Cerbuna 12, 50009 Zaragoza, Spain*

[2] *Fundación ARAID, Avenida de Ranillas 1D, 50018 Zaragoza, Spain*

[3] *INFN-Sezione di Roma, Piazzale Aldo Moro 2, 00185 Roma, Italy*

[4] *Istituto di Fotonica e Nanotecnologie-CNR, Via Cineto Romano 42, 00156 Roma, Italy*

(Received 7 May 2018; revised manuscript received 3 October 2018; published 12 June 2019)

Phonon reflection and transmission at the interfaces plays a fundamental role in cryogenic particle detectors, in which the optimization of the phonon signal at the sensor (in case of phonon-mediated detectors) or the minimization of the heat transmission (when the detection occurs in the sensor itself) is of primary importance to improve sensitivity. Nevertheless, the mechanisms governing the phonon physics at the interfaces are still not completely understood. The two more successful models, the acoustic mismatch model (AMM) and diffuse mismatch model (DMM) are not able to explain all the accumulated experimental data and the measurement of the transmission coefficients between the materials remains a challenge. Here, we use measurements of the athermal phonon flux in aluminum kinetic inductance detectors (KIDs) deposited on silicon substrates following a particle interaction to validate a Monte Carlo (MC) phonon simulation. We apply the Mattis-Bardeen theory to derive the phonon pulse energy and timing from the KID signal and compare the results with the MC for specular AMM and DMM reflection, finding a remarkably good agreement for specular, while diffuse reflection is clearly disfavored. For an aluminum film of 60 nm and a silicon substrate of 380 μm, we obtain transmission coefficients Si-Al in the range 0.3–0.55 and Si-Teflon in the range 0.1–0.15.

DOI: 10.1103/PhysRevApplied.11.064025

I. INTRODUCTION

Phonon-mediated cryogenic detectors using massive absorbers are a mature technology extensively employed in rare-event physics experiments, like neutrinoless double beta decay (0νDBD) searches [1] (see, for example, CUORE [2], CUPID-0 [3], LUMINEU [4], AMoRE [5], etc.) and dark matter direct detection experiments [6,7] (EDELWEISS [8], SuperCDMS [9], CRESST [10], etc.). Generally, the working temperature is <100 mK and the most common phonon sensors are neutron transmutation doped (NTD) Ge or ion-implanted Si thermistors [11], which are glued or bonded to the detector surface and depending on the gluing characteristics are more or less sensitive to the ballistic component, or transition edge sensors (TESs) [12], which usually are sensitive to the ballistic phonons. Currently, other kinds of sensors are being developed, such as metallic magnetic calorimeters (MMCs) [13] or kinetic inductance detectors (KIDs), the ones used in this work [14]. In all cases, low-threshold detection and/or identification of the event topology (multisite event, bulk versus surface, etc.) and nature of the interacting particle (α, β/γ, nuclear recoil, etc.) are mandatory. Hence, a good understanding of the phonon transport mechanism and heat losses in the interfaces is fundamental. On the other hand, a good understanding of these processes could also be useful to mitigate the effects of unwanted phonon-mediated signals. This is the case of cryogenic bolometers employed for cosmic microwave background measurements in space, which are severely affected by cosmic rays [15,16], and superconducting qubits, where phonons generated by cosmic rays and natural radioactivity can modify the qubit state [17,18].

Monte Carlo (MC) simulation of particle transport and interactions in matter is one of the basic ingredients for the design of a particle detector and the detection efficiency calculation. In particular, the GEANT4 package [19], initially developed for high-energy physics, now is used by a much wider community, including those working in astroparticle, space, and medical physics. Nevertheless, at the level of phonon physics, despite the fundamental role that phonons play in the energy collection in cryogenic bolometers, there is no generalized use of this analysis tool. Recently GEANT4

*mariam@unizar.es

has incorporated condensed-matter-physics elements as phonon and electron-hole pairs, essential for a more complete understanding of a cryogenic detector. The code was first developed by the CDMS cryogenic dark matter experiment [20] and subsequently integrated into GEANT4 as a general open-source package called G4CMP (GEANT4 Condensed Matter Physics) [21,22]. It has been validated for germanium, reproducing quite accurately the results of some experiments using heat pulses (produced, for example, by a focused laser beam) to excite ballistic phonons [23] and also giving a good description of the CDMS detectors: Ge cylinders with interleaved ionization and grounded phonon electrodes coupled to tungsten TESs to read the phonon signal. The MC simulation reproduces the arrival time of the ballistic phonons into the TESs and the energy partition between the phonon and charge [24,25].

A correct treatment of the phonon scattering and transmission at the interfaces is a main ingredient of the simulation when the sensitive area is a small fraction of the total detector surface. Nevertheless, phonon scattering at the interfaces is still an open question and there is no general agreement about the model to describe the experimental data, the most well-established ones being the acoustic mismatch model (AMM) and the diffuse mismatch model (DMM) [26]. AMM, which proposes specular reflection on the interface in analogy with the Snell's law for light, has been very successful at low temperatures [27], while DMM, in which phonons undergo diffuse reflection, is sensitive to surface roughness and preferred at temperatures above 1 K [28]. G4CMP includes a basic implementation of the phonon reflection mechanism based on these models in which a phonon in the boundary undergoes a reflection [specular for the AMM model or diffuse (Lambertian) for the DMM model] or is transmitted through the boundary with a certain probability given by a transmission coefficient, but the experimental determination of the phonon transmission coefficients at the interfaces is a hard task and currently large uncertainties exist.

In this work, we apply the G4CMP package to model two prototypes of the CALDER project [29], which is part of the research and development activities under development for the future upgrade of CUORE (the first ton-scale cryogenic detector in operation looking for 0νDBD [2]). The CALDER goal is to develop large-area high-sensitivity light detectors able to measure the very weak Cherenkov light that follows a 0νDBD event, so that we can distinguish a 0νDBD event from other backgrounds. The light is detected by superconducting KIDs of a few mm^2 of active area, deposited on a substrate of several cm^2. The substrate acts as a light absorber and generates phonons that will be absorbed in the superconductor and produce a signal. The main advantage of using KIDs for this study is that their response can be modeled as a function of measurable parameters of the Mattis-Bardeen theory, so we are able to estimate the total energy transformed into quasiparticles and make a direct comparison with the MC results. In addition, the small fractional area covered by the sensors with respect to the total absorber area enhances the influence of the phonon reflection and transmission model in the final results.

We apply the G4CMP package to a silicon wafer read by one or several KIDs. Comparing the simulation results with our data, we find a notable agreement for the AMM model and we are able to estimate the transmission coefficients at the interfaces Si-Al ($T_{\mathrm{Si}\to\mathrm{Al}}$) and Si-Teflon. The results that we present here can be extended to other kinds of detectors based on thin Al sensors.

The structure of the paper is as follows. Section II presents a brief description of the main physics ingredients included in the MC code and the parameters used in our implementation. Section III describes the general aspects of our detectors, experimental setup, data analysis, and the specific experimental configurations simulated. The details of the MC simulation are outlined in Sec. IV, while in Sec. V we compare the MC results with the experimental data and make an estimation of the relevant parameters. Finally, we present the summary in Sec. VI.

II. PHONON PHYSICS

In this section, we describe the basic phonon physics mechanisms implemented in the MC simulation, referring to Refs. [21,30] for a more complete description. Table I reports the numerical parameters used in our simulation, whose meaning is given in the following.

In a phonon-mediated cryogenic detector, particles (optical photons in our case) hitting the absorber produce optical phonons that decay promptly to the acoustic branch, producing an athermal population of high energy. The interaction length of these energetic phonons is very short, so they propagate quasidiffusively, with numerous changes in direction and polarization mode as they decay to lower-energy states. When the phonon energy drops sufficiently, its mean free path becomes larger than the dimensions of the crystal and it propagates following almost straight lines at the speed of sound in the material, a state that we call ballistic. If the dimensions of the sensor are small compared to the absorber size, as for CALDER detectors, ballistic phonons can undergo a large number of reflections at the substrate faces before reaching the KID, where they have a certain probability $T_{\mathrm{Si}\to\mathrm{Al}}$ of being absorbed or escaping detection (i.e., they are thermalized in the substrate or absorbed at the supports or the feedline).

Phonon tracking in crystalline structures strongly differs from the usual particle propagation in GEANT code because (1) an acoustic phonon can be in three different polarization states, one longitudinal (L) and two transversal, fast (FT) and slow (ST), with different velocities for every state; (2) the direction of energy propagation, which

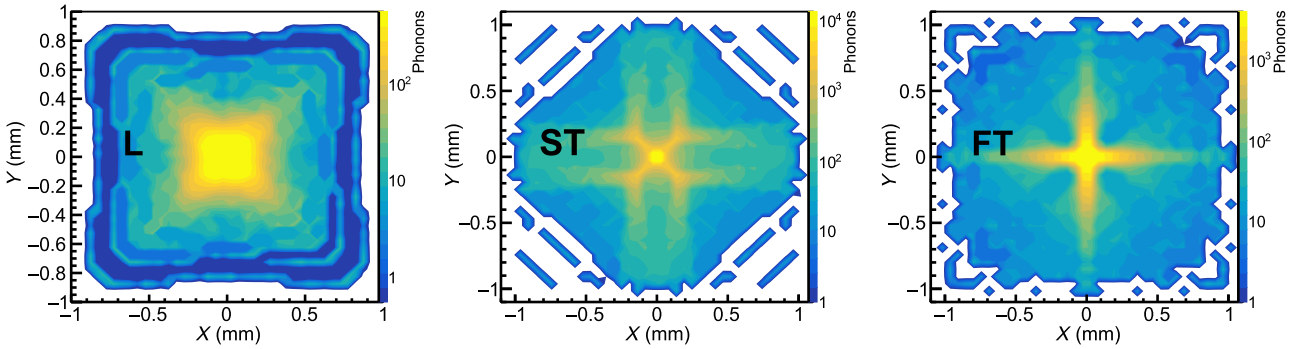

FIG. 1. Simulation of 0.1-THz phonons generated in one small spot of the Si wafer surface and detected in the opposite face. The panels show the flux intensity for every polarization: L (left), ST (center), and FT (right). The image spans an angle of $\pm 72^{\circ}$. Phonon focusing structures (bright colors) are clearly formed, especially for ST and FT modes.

occurs along the group velocity vector, $\nabla_k \omega(\mathbf{k})$, where ω is the phonon frequency, does not flow in general parallel to the wave-vector direction $\mathbf{k}$. This fact, which depends on the crystal lattice symmetry and physical properties (mainly, the elastic constants), causes the phonons to travel in preferred directions along the crystal, a phenomenon known as "phonon focusing" [36,37]. Silicon has a face-centered cubic crystal structure for which we expect quasi-isotropic transport for longitudinal phonons, but a highly anisotropic one for the transversal modes. To check that the caustics are correctly generated in our code, we perform a simulation starting with low-energy phonons of around 0.1 THz produced in a small spot at the surface of the Si wafer. Phonons of this frequency are ballistic in Si, so they propagate along an almost unchanged trajectory and polarization state until they reach the opposite face, forming the characteristic phonon focusing structures observed in Si by laser-beam experiments [38] (see Fig. 1).

The phonon propagation in the crystal is mainly governed by two processes:

(1) Isotopic scattering: When the substrate is composed of different isotopes, as is usually the case, there is a disruption in the propagation path that causes the phonon to scatter off and change direction with no energy loss. The energy-dependent rate is modeled as $R_I \nu^4$, where R_I depends on the material (see Table I) and $\nu = \omega/2\pi$ is the phonon frequency. The single scattering process depends on the inner product of the polarization vectors of the initial and final phonons, but the total expected rate is isotropic. Thus, the isotropic approximation in which the scattered

TABLE I. Parameters of the G4CMP Monte Carlo simulation. Unless otherwise stated, their values are for Si.

Symbol	Parameter description	Value	Ref.
d	Density	2.33 g/cm^3	[31]
C_{11}	Elastic constant	165.6 GPa	[32]
C_{12}	Elastic constant	63.9 GPa	[32]
C_{44}	Elastic constant	79.5 GPa	[32]
β	Second order elastic constant	−42.9 GPa	[31]
γ	Second order elastic constant	−94.5 GPa	[31]
λ	Lamé constant	52.4 GPa	[31]
μ	Lamé constant	68.0 GPa	[31]
DOS(L)	Density of states L	0.093	[33]
DOS(FT)	Density of states FT	0.376	[33]
DOS(ST)	Density of states ST	0.531	[33]
R_A	Anharmonic decay rate	7.41×10^{-56} s^4	[34]
R_I	Isotopic scattering rate	2.43×10^{-42} s^3	[34]
ν_{Debye}	Debye frequency	15 THz	[32]
η_{pb}	Pair-breaking efficiency	0.57	[35]
ξ_{tr}	Fraction of phonons tracked	0.02	
$n_{\text{refl}}^{\text{max}}$	Maximum number of reflections	1000	
$T_{\text{Si}\to\text{Al}}$	Si-Al transmission coefficient	0.1–1	
$T_{\text{Si}\to\text{Tef}}$	Si-Teflon transmission coefficient	0.1–1	

phonon has random direction and polarization distribution according to the density of states (DOS) is pretty accurate after several scatters and much less time consuming.

(2) Anharmonic decay: Because of nonlinear terms in the elastic coupling between adjacent lattice ions, a phonon spontaneously splits into two (or more) lower-frequency ones, with a rate that depends on the phonon frequency as $R_A\nu^5$, where R_A is a material-dependent constant (see Table I). A complete treatment of the scattering process is computationally too expensive, so usually the isotropic approximation, in which only L phonons can decay via $\mathrm{L} \rightarrow \mathrm{L} + \mathrm{T}$ and $\mathrm{L} \rightarrow \mathrm{T} + \mathrm{T}$ processes, where T is a generalization of FT or ST, is adopted.

As said before, there is not yet a complete understanding of the mechanisms that govern the phonon physics at the interfaces. Ideally phonons reflect and transmit conserving the energy and the component of **k** parallel to the interface, but polarization conversion can occur, being in general three reflected waves (trirefringence) and at most two transmitted ones (birefringence) [39]. The AMM and DMM models are the most extended but none of them is sufficient to entirely explain the experimental data.

III. PHONON-MEDIATED KINETIC INDUCTANCE DETECTORS

The KIDs operation principle is based on the properties of a superconducting film biased with ac (microwave) current. The inertia of Cooper pairs to momentum change produces an additional inductance, called kinetic inductance (L_{KI}), which depends on the density of Cooper pairs, and that can be measured by embedding the superconductor in a resonant *RLC* circuit with resonant frequency $\nu_0 = 1/2\pi\sqrt{LC}$. An energy release larger than twice the superconductor gap Δ (about 200 μeV for thin Al films) breaks Cooper pairs into quasiparticles, modifying both the residual resistance due to quasiparticles (the only dissipative term in the *RLC* resonant circuit) and the inductance due to Cooper pairs and changing the amplitude and phase of a microwave signal transmitted past the circuit. By slightly modifying the capacitance of every resonator, we can make them resonate at close but different frequencies, and in that way many of them can be read with the same line.

The detector used in this work follows a lumped-element KID (LEKID) design [40] that uses a separate meander section (inductor) and an interdigital capacitor to form a resonator coupled (inductively or capacitively) to a coplanar waveguide (CPW) for excitation and readout. They are fabricated at Istituto di Fotonica e Nanotecnologie of CNR (Rome). They are patterned by electron beam lithography in a 60-nm Al film deposited by an electron-gun evaporator on a thin (approximately 300 μm) high-resistivity Si(100) substrate [41,42]. In order to reduce the thermal quasiparticle population, we operate the detector well below the Al critical temperature. The Si wafer is fixed to a copper holder by small Teflon supports that act as a thermal link to the heat sink while the holder is anchored to the coldest point of a dilution refrigeration, at a base temperature of about 20 mK.

KIDs are excited with a fixed-frequency signal typically in the few-GHz range. After transmission through the device, the signal S_{21} is amplified by a CITLF4 SiGe cryogenic low-noise amplifier (with noise temperature $T_N \sim 7$ K) operated at 4 K and the rest of the electronics are at room temperature [29].

The signal transmitted through the feedline can be written as a function of the frequency ν as follows:

$$S_{21}(\nu) = I + iQ = 1 - \frac{Q/Q_c}{1 + 2iQ\dfrac{\nu - \nu_0}{\nu_0}}, \qquad (1)$$

where S_{21} is the forward scattering amplitude in the standard scattering matrix representation; I and Q indicate real and imaginary part of S_{21}; and Q is the quality factor of the resonant circuit, which is given by the addition in parallel of the coupling quality factor Q_c (that account for losses through the coupling) and the internal quality factor Q_i (dissipation due to quasiparticles and all other losses), so that $Q^{-1} = Q_c^{-1} + Q_i^{-1}$. When ν sweeps around the resonance, the signal traces out a circle in the IQ plane of diameter equal to Q/Q_c (see the inset of Fig. 2). We determine the circle center and radius, taking into account distortions introduced by the power stored in the resonator and possible impedance mismatches [43], to translate the $I(t)$ and $Q(t)$ components into phase $\delta\phi(t)$ and amplitude

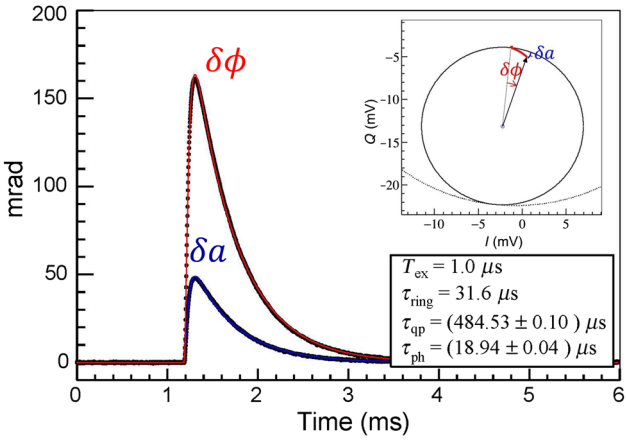

FIG. 2. $\delta\phi$ and δa pulse time evolution following an energy deposition of 36 keV in the Si substrate. The signals are fitted to the pulse shape of Eq. (3), taking also into account $T_{\mathrm{ex}} = 1$ μs (in red for $\delta\phi$ and blue for δa). The χ^2/NDF for the fit in the $\delta\phi$ component is 2.5. The resulting $\delta\phi$ fit parameters are shown in the legend. Inset: Resonance circle that we calibrate to obtain $\delta\phi$ and δa components from the real and imaginary parts of the S_{21} signal.

$\delta a(t)$ variations relative to the center of the resonance loop (calibration).

Once the resonance is calibrated, we choose the most sensitive frequency (or frequencies, in the case of reading several KIDs through the same line) and excite the resonators at an adequate power level [44]. We run an amplitude threshold trigger algorithm on the continuously acquired signals to capture particle passages through the detector and register a window of configurable length around the position of each trigger. Figure 2 shows a typical response to a 36-keV energy deposit in the Si substrate. The $\delta\phi(t)$ component usually features much better signal-to-noise ratio (SNR) than $\delta a(t)$, so in the following we use only this signal.

A. Phonon time constant

Athermal phonons arrive to the KIDs with a characteristic time distribution that depends on the detector material and geometry. In general, it can be modeled by two time constants, accounting for the pulse rise ($\tau_{\rm ph}^{\rm rise}$) and decay ($\tau_{\rm ph}$), so the number of phonons at the KID can be written as

$$N_{\rm ph}(t) = \frac{N_{\rm ph}}{\tau_{\rm ph} - \tau_{\rm ph}^{\rm rise}}\left(e^{-t/\tau_{\rm ph}} - e^{-t/\tau_{\rm ph}^{\rm rise}}\right). \qquad (2)$$

When $\tau_{\rm ph}^{\rm rise} \ll \tau_{\rm ph}$, as in the case of the detectors analyzed in this work, the expression (2) can be approximated by a single exponential with constant $\tau_{\rm ph}$.

In order to infer $\tau_{\rm ph}$ from the KID signal, we have to disentangle the contribution of other temporal constants. (i) At the KID, phonons break Cooper pairs and generate quasiparticles with a probability given by the pair-breaking efficiency $\eta_{\rm pb}$ (see Table I), which recombine again into Cooper pairs with lifetime $\tau_{\rm qp}$. The recombination rate depends not only on superconductor properties, but also on the quasiparticle density and, consequently, on temperature and microwave power ($P_{\mu\rm w}$) [45]. (ii) The Q factor determines the time constant at which the power dissipation decays as $\tau_{\rm ring} = Q/\pi\nu_0$. Hence, high-$Q$ resonators are more sensitive but are also slower. The temporal evolution of the signal is a convolution of these effects:

$$\delta\phi(t) = \Phi_{\rm qp}\tau_{\rm qp}\left[\frac{\tau_{\rm qp}e^{-t/\tau_{\rm qp}}}{(\tau_{\rm qp}-\tau_{\rm ph})(\tau_{\rm qp}-\tau_{\rm ring})} + \frac{\tau_{\rm ph}e^{-t/\tau_{\rm ph}}}{(\tau_{\rm ph}-\tau_{\rm qp})(\tau_{\rm ph}-\tau_{\rm ring})} + \frac{\tau_{\rm ring}e^{-t/\tau_{\rm ring}}}{(\tau_{\rm ring}-\tau_{\rm qp})(\tau_{\rm ring}-\tau_{\rm ph})}\right], \qquad (3)$$

where $\Phi_{\rm qp}$ is the pulse integral and its expression is derived in the next section.

As we explain in the next section, we excite the substrate by a light-emitting diode (LED) pulse whose duration $T_{\rm ex}$ is of the order of a few μs, so the final waveform results from the convolution of Eq. (3) with a rectangular function of length $T_{\rm ex}$.

For every acquired signal, we fit the $\delta\phi$ pulse evolution to the pulse shape described above, fixing $\tau_{\rm ring}$ to the value corresponding to the measured Q factor. In this way, we obtain $\tau_{\rm ph}$ that we compare with the MC results. Superimposed to the pulses of Fig. 2, we show the results from the fit for the $\delta\phi(t)$ and $\delta a(t)$ signals.

B. Response to energy absorption

We can relate the energy release in the substrate E to the energy absorbed at every resonator $E_{\rm abs}$ through an efficiency factor η, so that $E_{\rm abs} = \eta E$. The efficiency can be factorized as $\eta = \eta_{\rm KID}\eta_{\rm pb}$, where $\eta_{\rm KID}$ depends on the geometry of the detector and the transmission coefficients at the interface, and $\eta_{\rm pb}$ is the pair-breaking efficiency in Al. We take $\eta_{\rm pb}$ as approximately 0.57, while $\eta_{\rm KID}$ is the parameter that we shall extract from the MC simulation, and $\eta_{\rm pb}$ is the pair-breaking efficiency in Al, which we take as approximately 0.57 [35]. Now, $\Phi_{\rm qp}$ in Eq. (3) represents the overall change in $\delta\phi$ corresponding to an increment in the quasiparticle population $N_{\rm qp} = E_{\rm abs}/\Delta = \eta E/\Delta$, that can be calculated from the Mattis-Bardeen theory in the thin-film limit. After some analytical approximations [46], we can write

$$\Phi_{\rm qp} = \frac{\alpha S_2(\nu, T_{\rm qp})Q}{N_0 V\Delta(T_{\rm qp})}\frac{\eta E}{\Delta(T_{\rm qp})}, \qquad (4)$$

where N_0V is the single spin density of states at the Fermi level (1.72×10^{10} eV^{-1} μm^{-3} for Al [14]) multiplied by the active volume of the resonator; α is the fraction of kinetic inductance $L_{\rm KI}/L$; $T_{\rm qp}$ is the effective temperature of the quasiparticle system, larger than the sink temperature due to $P_{\mu\rm w}$; and S_2 is a dimensionless factor given by the Mattis-Bardeen theory. The parameters Δ, α, S_2, and Q are measurable quantities for a given $P_{\mu\rm w}$; therefore, from the pulse fit, we can obtain $\Phi_{\rm qp}$ and determine through Eq. (4) the efficiency η of every pixel in order to compare with the MC results.

C. Experimental configurations

We study two different detector configurations with different KID characteristics and layout.

The first prototype (P1 in the following) consists of a single KID lithographed on a 380-μm-thick Si substrate with a size of 2×2 cm^2. Figure 3 shows a picture of the detector mounted in the copper holder (left panel) and a schematic design of the single KID (right panel). The inductor section is a meander of 30 strips of 62.5 μm $\times$ 2 mm, with gap of 5 μm between them, and the capacitor is composed of only two fingers. The total active area is 4.0 mm^2, excluding the gaps and including the active

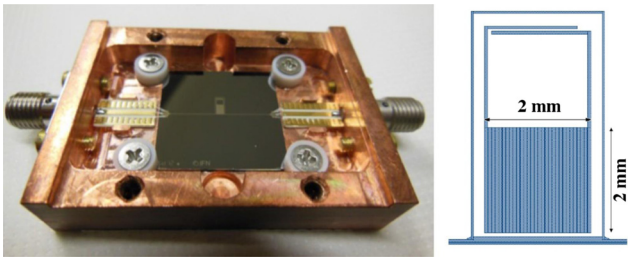

FIG. 3. Left: Picture of the P1 prototype: A 60-nm-thick Al KID deposited on a 2 × 2-cm^2, 380-μm-thick Si substrate. Four Teflon supports, one at each corner, fix the detector to a copper holder that is anchored to the cryostat. Right: Geometry of the single pixel: an inductor made of 30 strips with a size of 62.5 μm × 2 mm, with a gap of 5 μm between them, and a capacitor composed of two fingers.

region that connects the inductor to the capacitor. The feedline is a 72-μm-width CPW that cuts across the Si substrate from side to side. The pixel and feedline are made of 60-nm-thick Al. Four cylindrical Teflon supports, one at each corner of the substrate, fix the detector to a copper holder that is anchored to the cryostat. The contact area between Si and Teflon is lower than 3 mm^2 at every support. For detailed results of this prototype, see Ref. [44].

In the second prototype, that we label as P4 (see Fig. 4), the wafer is 375 μm thick and there are four Al KIDs with an inductive meander made of 14 connected strips with a size of 80 μm × 2 mm closed by a capacitor made of 5 interdigitated fingers with a size of 1.4 mm × 50 μm. The active area of the single pixel is 1.15 × 2 mm^2. The feedline is a 420-μm-width and 60-nm-thick CPW.

Compared to P1, P4 has a smaller contact area between Si and Teflon, as it is held by only two supports at opposite edges in the middle of the substrate. The contact area at

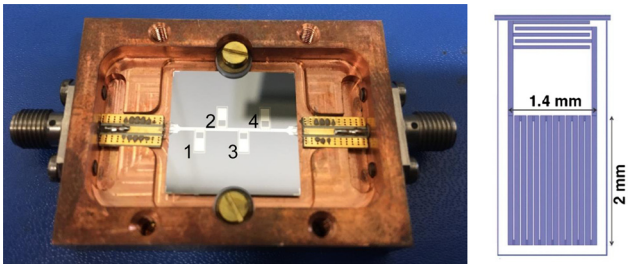

FIG. 4. Left: Picture of the P4 prototype. Four Al KIDs are deposited on a 300-μm-thick Si substrate with a size of 2 × 2 cm^2. Two cylindrical Teflon supports with a contact area of around 3 mm^2 each hold the substrate in the copper structure. Right: Geometry of the single pixel (60-nm-thick Al film): an inductive meander with 14 connected strips with a size of 80 μm × 2 mm and capacitor made of 5 interdigitated fingers with a size of 1.4 mm × 50 μm. The active area of the single pixel is 1.15 × 2 mm^2.

every support is about 3 mm^2, so the total interface Si-Teflon is halved with respect to P1. In turn, the feedline is approximately 6 times wider.

We operate both prototypes as described at the beginning of this section. The first step is to select the excitation power $P_{\mu w}$. High powers feature in general a better SNR, as the noise in our setup is dominated by the amplifier and goes with $1/\sqrt{P_{\mu w}}$, but as we raise $P_{\mu w}$, the resonances show an increasing distortion and the relationship of Eq. (4) is no longer valid [44]. Therefore, we perform a power scan and select the largest $P_{\mu w}$ before distortion.

For every prototype, we measure the parameters that enter in Eq. (4) and report their values at the selected $P_{\mu w}$ in Table II. The Q, Q_i, and Q_c factors are computed by fitting the resonance circle as described in Ref. [43]. We determine the critical temperature T_c (that for thin films depends on thickness and other parameters, as the quality of the deposition) during the cooling-down and infer Δ_0 from BCS theory. Then, we compute α from the resonant frequency shift as we increase the thermal quasiparticle density by increasing the base temperature of the system. We fit the resulting curve to the Mattis-Bardeen theory prediction [47], keeping Δ_0 fixed in the fit. For the P4 prototype, we average the results of the four resonators.

The detectors are illuminated on the back of the substrate by an optical fiber coupled to a fast warm LED (λ = 400 nm). The LED equivalent energy is calibrated with a photomultiplier and the calibration is checked at very low intensity by photon counting Poisson statistics [48]. In Table II, we report also the source position with respect to the center of the substrate, the diameter of the illuminated spot (ϕ), and the optical pulse duration.

We take $\mathcal{O}(2000)$ LED pulses for every configuration. In order to improve the SNR, we apply a software low-pass filter with a 100-kHz cutoff whose effect is included in the pulse fitting. Finally, we average the pulses and perform a fit as described in Sec. III A to obtain τ_{ph} and η. We report the results for each KID in Table III.

The error in η is dominated by the systematic error in Δ_0 and α. For τ_{ph}, in addition to the statistical error of the fit, we estimate a systematic one by starting from different sets of initial fit parameters and by taking pulses with different T_{ex} ranging from 1 to 10 μs. The χ^2/NDF values of the fits range between 1 and 3.5 for all the KIDs except for KID3, for which we obtain values between 4 and 6.8. In the P4 prototype, there is a very small (approximately 200 μm) rightward shift of the KIDs layout with respect to the center of the substrate. It is not appreciable in Fig. 4, but it is responsible for the slight (approximately 7%) larger efficiency of KIDs 1 and 2 with respect to KIDs 3 and 4, as they are slightly closer to the source. The simulation also includes the shift, so we expect to observe this small effect in the MC results as well.

TABLE II. Experimental relevant parameters of the simulated experiments with P1 and P4 prototypes. See text for details.

Prototype	Coupling	T_c (K)	Δ_0 (μV)	α (%)	$P_{\mu v}$ (dBm)	KID	Q (k)	Q_i (k)	Q_c (k)	$\tau_{\rm ring}$ (μs)	Source Position (mm)	Source ϕ (mm)	Source $T_{\rm ex}$ (μs)
P1	Inductive	1.180 ± 0.020	179 ± 3	$2.54 \pm 0.9_{\rm stat} \pm 0.26_{\rm syst}$	-76.8	1	149	2301	159	18.2	$(0, -6)$	4.66	10
P4	Capacitive	1.300 ± 0.025	197 ± 4	$2.14 \pm 0.04_{\rm stat} \pm 0.27_{\rm syst}$	-79.1	1	18.6	69.7	25.4	2.23	(0, 0)	4.66	1
						2	38.4	99.6	62.4	4.59			
						3	138	899	162	16.4			
						4	266	407	772	31.6			

IV. G4CMP MC IMPLEMENTATION

The G4CMP package simulates (i) the generation of acoustic phonons and electron-hole pairs in a material after an energy deposition; (ii) their propagation in the media, anisotropic according to the material elastic constants for phonons and driven by an electric field for the charge; (iii) the two principal phonon scattering processes described in Sec. II with isotropic approximation; and (iv) a simplified implementation of the reflection and transmission mechanisms at interfaces, in which the multirefringence is not considered: the phonon is transmitted through the boundary with a probability given by the transmission coefficient, or it is reflected back, following a specular reflection for the AMM model or a Lambertian one for DMM. So, in the current implementation, no mode conversion occurs.

In our simulation, as no electric field is applied to the detector, the charge is not taken into account and all the energy of the interaction goes to the phonon channel. Following a photon absorption in the Si substrate, acoustic phonons are generated isotropically along the incident particle track. The energy distribution of the primordial phonons is unknown; nevertheless, their effects are wiped out after the quasidiffusion stage, so we take the Debye energy (approximately 62 meV in Si) as the starting point and select the polarization L, FT, or ST randomly according to the DOS in the material. The history of every phonon is followed recording its polarization, ω, and $\mathbf{k}$ until one of the following conditions is verified: (i) it is absorbed in Al (KIDs or feedline) or Teflon, (ii) its energy drops below 2Δ, or (iii) a predefined number of reflections $n_{\rm refl}^{\rm max}$ is reached.

TABLE III. Experimental results of the P1 and P4 prototypes. For every KID, we report the efficiency η and the characteristic phonon arrival time $\tau_{\rm ph}$.

Prototype	KID	η (%)	$\tau_{\rm ph}$ (μs)
P1	1	13.3 ± 1.1	$25.4 \pm 0.1_{\rm stat} \pm 0.2_{\rm syst}$
P4	1	2.9 ± 0.3	$16.8 \pm 1.4_{\rm stat} \pm 2.3_{\rm syst}$
	2	6.7 ± 0.7	$8.64 \pm 0.14_{\rm stat} \pm 0.84_{\rm syst}$
	3	6.2 ± 0.7	$9.09 \pm 0.05_{\rm stat} \pm 0.56_{\rm syst}$
	4	2.7 ± 0.4	$15.5 \pm 0.5_{\rm stat} \pm 2.8_{\rm syst}$

We simulate a simplified geometry of the detector with four main components: Si wafer, Teflon supports, the feedline, and the KIDs, the latter two components both being made of Al (see Fig. 5). For the sake of keeping the simulation computing time at a reasonable level, only a certain fraction of the phonons $\xi_{\rm tr}$ are tracked (see Table I) and the final results are scaled with this value. In order to determine the effect of the reflection model and transmission coefficients, we generate a batch of simulations spanning $T_{\rm Si\to Al}$ and $T_{\rm Si\to Tef}$ from 0.1 to 1, for both models. It is worth mentioning that the code does not implement phonon propagation in Al, so a phonon absorbed in the KIDs generates a signal with probability $\eta_{\rm pb}$ or is killed. Hence, $(1-T_{\rm Si\to Al})$ includes the probability of a phonon to enter the Al and to be reflected back to the Si substrate.

A single simulation event starts with the generation of about 10^4 optical photons ($\lambda = 400$ nm), uniformly distributed at the 4.66-mm-diameter fiber spot, that are stopped in the first micron of the Si substrate at the face opposite to the KIDs. The spot is centered in the middle of the substrate in the P4 simulation, while for P1 it is shifted 6 mm away from the KID in the vertical direction, and the photons are distributed in time according to a square pulse of duration $T_{\rm ex}$ (see Table II). For every configuration, we generate between 20 and 50 single events. The outputs of the simulation are the time, energy, position,

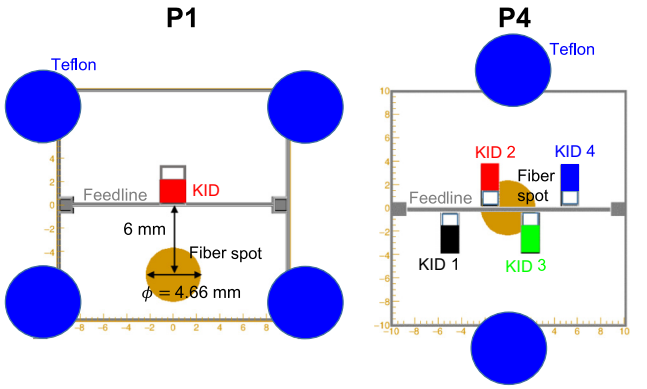

FIG. 5. A sketch of the main components included on the MC simulation of the prototype P1 (left) and P4 (right). In both cases, the fiber spot (brown) has a diameter of 4.66 mm and fires on the opposite side of the KIDs.

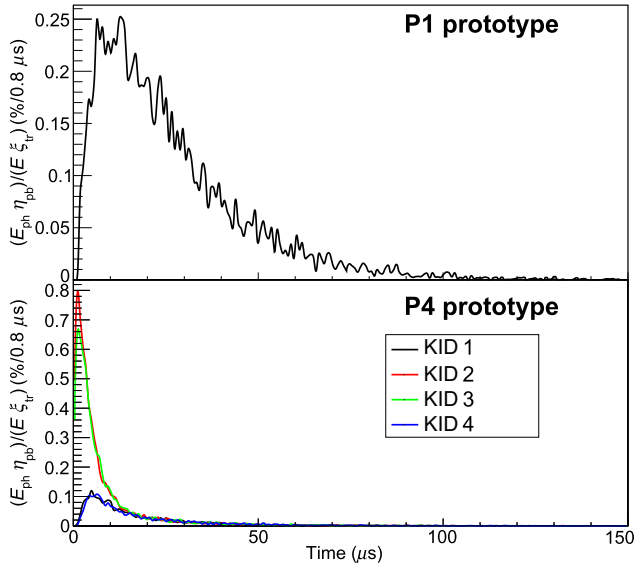

FIG. 6. Phonon distribution at the KIDs for P1 (upper panel) and P4 (bottom panel), corresponding to the AMM model, $T_{\mathrm{Si}\to\mathrm{Al}} = 0.36$, and $T_{\mathrm{Si}\to\mathrm{Tef}} = 0.4$.

and polarization of every phonon absorbed in the Teflon, the feedline, or the KIDs.

V. RESULTS AND DISCUSSION

For each fiber event in the wafer, we construct the phonon pulse evolution for every time and integrate it to obtain the total energy absorbed in the simulation at every KID, which we denote as ΔE_{ph}. Then, we scale with the number of tracked phonons ξ_{tr} and the pair-breaking efficiency η_{pb} to calculate the absorbed energy and we divide by E to obtain the efficiency in a single KID as

$$\eta = \frac{1}{E}\frac{\eta_{\mathrm{pb}}}{\xi_{\mathrm{tr}}}\Delta E_{\mathrm{ph}}. \tag{5}$$

Figure 6 displays one such event for the AMM model, $T_{\mathrm{Si}\to\mathrm{Al}} = 0.36$, and $T_{\mathrm{Si}\to\mathrm{Tef}} = 0.4$ for both prototypes. The simulation does not include resonator-related time constants (τ_{ring},τ_{qp}), so the pulse shape is described by Eq. (2). The rise time of the phonon pulses is around 1 order of magnitude smaller than the decay time, so we consider only one time constant τ_{ph} calculated as $T_{\mathrm{ph}}^{10-90}/2.2$, where T_{ph}^{10-90} is the 90th minus the 10th percentile of the phonon distribution.

We observe no substantial variations in arrival time among the three polarizations, despite their different velocities (approximately 9000 m/s longitudinal and 5400 m/s for the transversal modes) since modes are highly mixed as a consequence of the scattering processes. For example, for the P1 pulse in Fig. 6, we obtain $\tau_{\mathrm{ph}} = (21.3, 21.3, 21.0)$ μs for the (L, FT, ST) components separately and $\tau_{\mathrm{ph}} = 21.2$ μs for the three modes together.

The choice for the $n_{\mathrm{refl}}^{\mathrm{max}}$ parameter is not of great importance in the final results: for the configurations with low values of the transmission coefficients ($T_{\mathrm{Si}\to\mathrm{Al}} \sim 0.2$, $T_{\mathrm{Si}\to\mathrm{Tef}} \sim 0.1$), only 1%–3% (0.1%–0.4%) of phonons undergo more than 200 (500) reflections. For values of $T_{\mathrm{Si}\to\mathrm{Al}}$ and $T_{\mathrm{Si}\to\mathrm{Tef}}$ around 0.4, the percentages are 0.5%–1% (0.05%–0.1%).

We also study the amount of phonon absorption at every material as a function of phonon frequency and show the results in Fig. 7 for the same configuration as Fig. 6. The geometric differences among the two prototypes described in Sec. III C (more Teflon in P1, an approximately 6 times wider feedline in P4) are clearly reflected in the simulation: while for P1 most of the phonons are absorbed in Teflon (about 60% of the total), in P4 the element that is taking the major part is the feedline (approximately 55%), followed by the KIDs (approximately 28%) and then the Teflon (approximately 17%). The maxima of the distributions are at phonon frequencies between 0.7 and 0.9 THz and they are slightly asymmetric, with positive skewness. When the origin of the phonon pulse is close to the

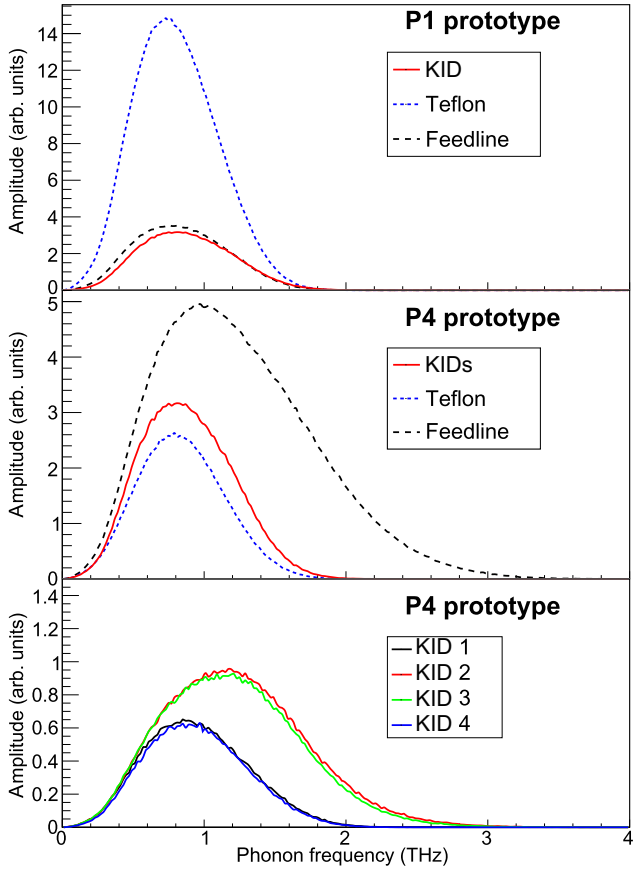

FIG. 7. Frequency distribution of the phonons absorbed in the different materials (Teflon, feedline, KIDs) for P1 (upper panel) and P4 (middle panel). In the bottom panel, the P4 distribution at every KID is plotted separately.

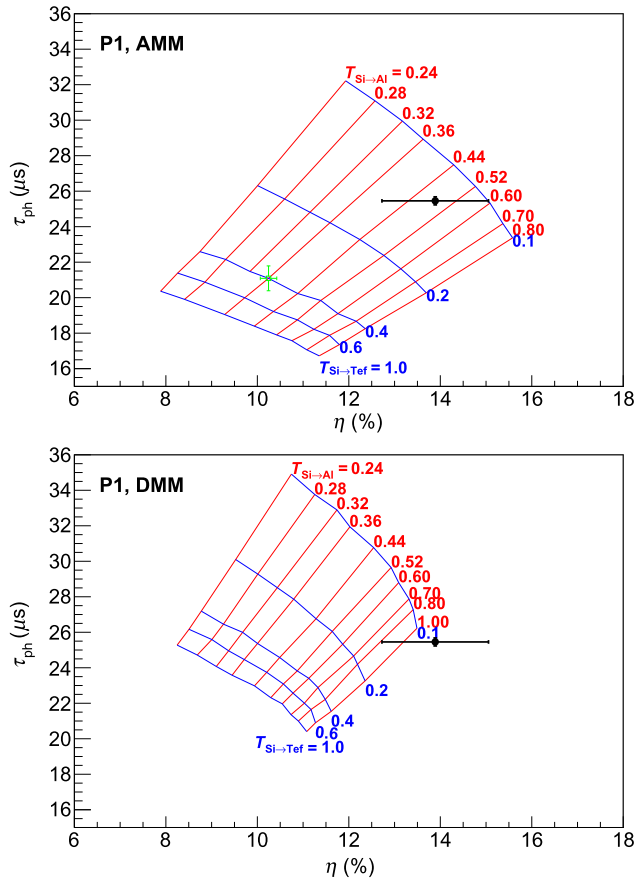

FIG. 8. Comparison of the MC results with experimental data for P1 prototype and AMM model (upper panel) or DMM model (bottom panel). The red (blue) lines correspond to simulations with constant values of the $T_{Si\to Al}$ ($T_{Si\to Tef}$) coefficient, while the points are taken from Table III. The green error bars represent the systematic uncertainty associated to the MC parameters.

absorbing element, as for the feedline and KIDs 2 and 3 in P4, the asymmetry is more pronounced with a longer tail to higher frequencies.

Finally, in Figs. 8 and 9, we compare the MC results with the experimental data. The red (blue) lines correspond to simulations with constant values of the $T_{Si\to Al}$ ($T_{Si\to Tef}$) coefficient, while the points are taken from Table III. In order to estimate a systematic error associated to the simulation, we identify the most sensitive parameters of the model to be the decay constants R_A and R_I and the elastic constants C_{11}, C_{12}, and C_{44}. We consider a variation of $\pm 5\%$ for the elastic constants [49–51] and $\pm 20\%$ for the decay constants and calculate the variation in τ_{ph} and η for some simulated configurations. The result for the AMM model in the configuration $T_{Si\to Al} = 0.36$ and $T_{Si\to Tef} = 0.4$ is a variation of $\pm 3\%$ in τ_{ph} and $\pm 2\%$ in η (green lines in Fig. 8). Similar results are obtained for other configurations. As regards the fraction of tracked phonons ξ_{tr}, increasing it from 2% up to 20% produces an error below 0.2%.

For P1, with one single KID, phonon pulses are faster and more energetic for larger $T_{Si\to Al}$ values. When we increase $T_{Si\to Tef}$ instead, they are also faster, but less energy is collected, as phonons are lost in Teflon. This rule no longer holds true when more than one KID is competing for the same energy deposition, as it is the case of P4: the sensors far from the source (KID1 and KID4 in Fig. 9) reverse behavior, and the collected energy is lower for larger values of $T_{Si\to Al}$ because it is being more quickly absorbed in the near KIDs and the feedline. The small shift in the KIDs position toward the right side of the wafer in P4 is also noticeable in the simulation and results in larger energy depositions in KID1 and KID2 compared to those of KID3 and KID4.

In general, simulations with the DMM model produce slower and less energetic phonon pulses than those with AMM, except when KIDs are very close to the phonon source, as it is the case of KIDs 2 and 3 in P4. An explanation for this behavior can be found in the very different propagation patterns that phonons follow once they enter the ballistic regime for specular or diffusive reflection. In our geometry, we observe a much larger density of phonon tracks in the central part of the wafer for the AMM simulation rather than for DMM. The origin of this different distribution could be, as pointed out by some authors [52], that phonon caustics survive up to some degree with the specular reflection, while a more homogeneous distribution of phonons is expected for a Lambertian reflection. For our geometry, the larger concentration of phonons in the central part of the wafer results in a more effective energy collection at the KIDs than in Teflon.

We obtain a consistent picture between data and simulation for both prototypes for the AMM model, while our experimental data cannot be modeled considering only diffuse reflection, unless extreme values of the transmission coefficients are introduced. In the case of P1 (the most sensitive probe for the reflection model, as the energy deposition is far away from the KID), for the same transmission coefficients, the DMM model produces phonon pulses between 2 and 4 μs slower. The very fast and energetic pulses measured in this setup cannot be reproduced by our simulation with DMM model unless a transmission coefficient of almost 1 is considered for $T_{Si\to Al}$.

The range of values of $T_{Si\to Al}$ that best describes the experimental data is 0.30–0.55. In the case of $T_{Si\to Tef}$, the P1 data point to the region 0.1–0.15; nevertheless, the P4 simulations do not impose a large constraint, as in general the whole $T_{Si\to Tef}$ range agrees with the experimental point at 1σ error as a result of the reduced Si-Teflon interface. At a closer look, the AMM P4 simulation could be affected by a systematic bias: in the MC, less energy is collected at the KIDs far from the source (KID1 and KID4) with respect to the measurement. This distance-dependent bias could suggest a deficiency of the model

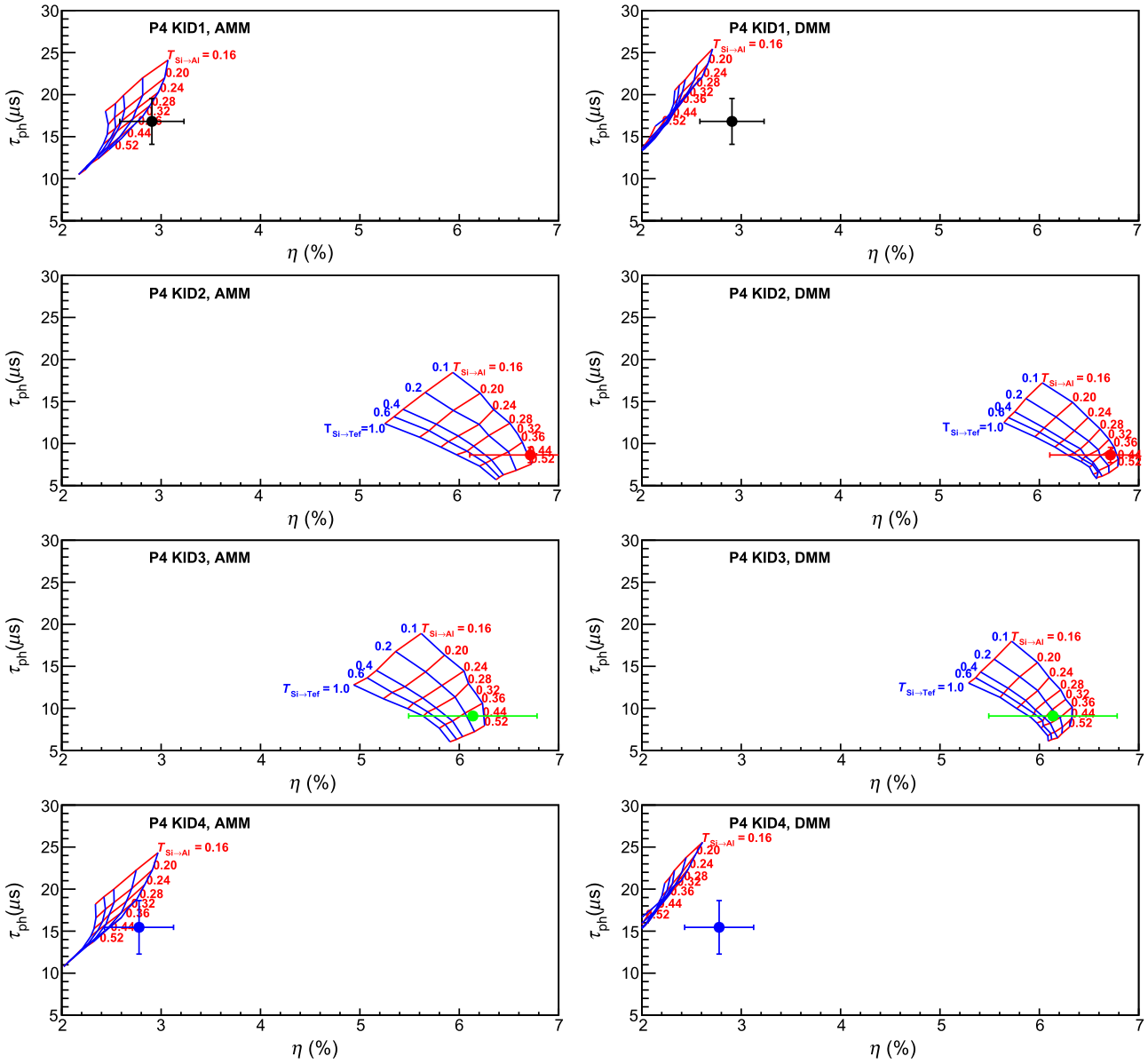

FIG. 9. Same as Fig. 8 for the four KIDs of P4.

that appears when the number of phonon reflections is large. This could be due to the simplification of the reflection mechanisms in the simulation, which currently do not include mode conversion, or other phenomena not considered in the present implementation. For example, a slight dependence of the transmission coefficients with phonon frequency would result in distinct absorption for far and near KIDs, as the phonon frequency distribution is different (see Fig. 7). A larger substrate and/or a different KID layout would be necessary to test this conjecture.

It is worth noting that, in general, we expect the phonon transmission coefficient to be dependent on the thickness for thin films. The experimental data presented here correspond to an Al thickness of 60 nm, and so does the $T_{Si\to Al}$ transmission coefficient that we determine. Future measurements with different films will allow us to study this dependency.

VI. CONCLUSION

We implement a phonon MC simulation based on the G4CMP extension of the GEANT4 code and applied it to model phonon-mediated cryogenic detectors with thin Si absorbers and an Al KID readout, clamped by Teflon supports to a dilution unit at about 20 mK. We perform two different experiments with different geometries and KID layouts and we compare the results with those of the MC simulations, considering two different reflection mechanisms at the interfaces (a specular reflection based on the AMM model and a diffuse one for the DMM model) and

transmission coefficients spanning from 0.1–1 for the Si-Teflon and Si-Al interfaces. We find a good agreement for transmission coefficients Si-Al in the range 0.3–0.55 and Si-Tef in the range 0.1–0.15 for the AMM model, while the simulation with diffuse reflection based on the DMM model does not provide a realistic description of our data. The Si-Al result is valid for an Al film with a thickness of 60 nm. We observe also a hint of a systematic bias in our simulation when the number of phonon reflections is large: simulated phonon pulses are less energetic than data. In the future, we will further investigate this issue with larger detectors. The results that we present are applicable to other cryogenic detectors with thin Al sensors.

ACKNOWLEDGMENTS

This work is supported by the European Research Council (FP7/2007-2013) under Contract No. CALDER 335359 and by the Italian Ministry of Research under the FIRB Contract No. RBFR1269SL. The authors thank the personnel of INFN Sezione di Roma for the technical support, in particular M. Iannone.

[1] S. Dell'Oro, S. Marcocci, M. Viel, and F. Vissani, Neutrinoless double beta decay: 2015 review, Adv. High Energy Phys. **2016**, 2162659 (2016).

[2] C. Alduino, F. Alessandria, K. Alfonso, E. Andreotti, C. Arnaboldi, F. T. Avignone III, O. Azzolini, M. Balata, I. Bandac, T. I. Banks, and G. Bari, First Results from CUORE: A Search for Lepton Number Violation via $0\nu\beta\beta$ Decay of ^{130}Te, Phys. Rev. Lett. **120**, 132501 (2018).

[3] O. Azzolini, M. T. Barrera, J. W. Beeman, F. Bellini, M. Beretta, M. Biassoni, C. Brofferio, C. Bucci, L. Canonica, S. Capelli, L. Cardani, P. Carniti, N. Casali, L. Cassina, M. Clemenza, O. Cremonesi, A. Cruciani, A. D'Addabbo, I. Dafinei, S. Di Domizio, *et al.*, First Result on the Neutrinoless Double-β Decay of ^{82}Se with CUPID-0, Phys. Rev. Lett. **120**, 232502 (2018).

[4] E. Armengaud, Q. Arnaud, C. Augier, A. Benoit, L. Bergé, R. S. Boiko, T. Bergmann, J. Blümer, A. Broniatowski, V. Brudanin, and P. Camus, Development and underground test of radiopure $ZnMoO_4$ scintillating bolometers for the LUMINEU $0\nu2\beta$ project, J. Instr. **10**, P05007 (2015).

[5] J. Y. Lee, V. Alenkov, L. Ali, J. Beyer, R. Bibi, R. S. Boiko, K. Boonin, O. Buzanov, N. Chanthima, M. K. Cheoun, and D. M. Chernyak, A study of radioactive contamination of $^{40}Ca^{100}MoO_4$ crystals for the AMoRE experiment, IEEE Trans. Nucl. Sci. **63**, 543 (2016).

[6] M. W. Goodman and E. Witten, Detectability of certain dark matter candidates, Phys. Rev. **D31**, 3059 (1985).

[7] L. E. Strigari, Galactic searches for dark matter, Phys. Rept. **531**, 1 (2013).

[8] L. Hehn, E. Armengaud, Q. Arnaud, C. Augier, A. Benoît, L. Bergé, J. Billard, J. Blümer, T. DeBoissiére, A. Broniatowski, and P. Camus, Improved EDELWEISS-III sensitivity for low-mass WIMPs using a profile likelihood approach, Eur. Phys. J. C **76**, 548 (2016).

[9] R. Agnese, T. Aramaki, I. J. Arnquist, W. Baker, D. Balakishiyeva, S. Banik, D. Barker, R. B. Thakur, D. A. Bauer, T. Binder, and M. A. Bowles, Results from the Super Cryogenic Dark Matter Search Experiment at Soudan., Phys. Rev. Lett. **120**, 061802 (2018).

[10] G. Angloher, A. Bento, C. Bucci, L. Canonica, X. Defay, A. Erb, F. vonFeilitzsch, N. F. Iachellini, P. Gorla, A. Gütlein, and D. Hauff, Results on light dark matter particles with a low-threshold CRESST-II detector, Eur. Phys. J. C **76**, 25 (2016).

[11] D. McCammon, in *Cryogenic particle detection*, edited by C. Enss (Springer, Berlin, Germany, 2005).

[12] K. D. Irwin, and G. C. Hilton, in *Cryogenic particle detection*, edited by C. Enss (Springer, Berlin, Germany, 2005).

[13] A. Fleischmann, C. Enss, and G. M. Seidel, in *Cryogenic particle detection*, edited by C. Enss (Springer, Berlin, Germany, 2005).

[14] P. K. Day, H. G. LeDuc, B. A. Mazin, A. Vayonakis, and J. Zmuidzinas, A broadband superconducting detector suitable for use in large arrays, Nature **425**, 817 (2003).

[15] A. Catalano, P. Ade, Y. Atik, A. Benoit, E. Bréele, J. J. Bock, P. Camus, M. Chabot, M. Charra, B. P. Crill, and N. Coron, Impact of particles on the planck HFI detectors: Ground-based measurements and physical interpretation, A&A **569**, A88 (2014).

[16] A. Catalano, A. Benoit, O. Bourrion, M. Calvo, G. Coiffard, A. D'Addabbo, J. Goupy, H. Le Sueur, J. Macías-Pérez, and A. Monfardini, Maturity of lumped element kinetic inductance detectors for space-borne instruments in the range between 80 and 180 GHz, A&A **592**, A26 (2016).

[17] K. Serniak, M. Hays, G. de Lange, S. Diamond, S. Shankar, L. D. Burkhart, L. Frunzio, M. Houzet, and M. H. Devoret, Hot Nonequilibrium Quasiparticles in Transmon Qubits, Phys. Rev. Lett. **121**, 157701 (2018).

[18] L. Grünhaupt, N. Maleeva, S. T. Skacel, M. Calvo, F. Levy-Bertrand, A. V. Ustinov, H. Rotzinger, A. Monfardini, G. Catelani, and I. M. Pop, Loss Mechanisms and Quasiparticle Dynamics in Superconducting Microwave Resonators Made of Thin-Film Granular Aluminum, Phys. Rev. Lett. **121**, 117001 (2018).

[19] S. Agostinelli, J. Allison, K. A. Amako, J. Apostolakis, H. Araujo, P. Arce, M. Asai, D. Axen, S. Banerjee, G Barrand, and F. Behner, GEANT4 – simulation toolkit, Nucl. Instr. Meth. A **506**, 250 (2003).

[20] R. Agnese, A. J. Anderson, M. Asai, D. Balakishiyeva, D. Barker, R. B. Thakur, D. A. Bauer, J. Billard, A. Borgland, M. A. Bowles, and D. Brandt, Improved WIMP-search reach of the CDMS II germanium data, Phys. Rev. **D92**, 072003 (2015).

[21] D. Brandt, R. Agnese, P. Redl, K. Schneck, M. Asai, M. Kelsey, D. Faiez, E. Bagli, B. Cabrera, R. Partridge, T. Saab, and B. Sadoulet, Semiconductor phonon and charge transport Monte Carlo simulation using Geant4 (2014), arXiv:1403.4984.

[22] R. Agnese, D. Brandt, M. Kelsey, and P. Redl, G4CMP – Geant4 add-on framework for phonon and charge-carrier physics, https://github.com/kelseymh/G4CMP.

[23] D. Brandt, M. Asai, P. L. Brink, B. Cabrera, E. Coutoe Silva, M. Kelsey, S. W. Leman, K. McArthy, R. Resch, D. Wright, and E. Figueroa-Feliciano, Monte carlo simulation of massive absorbers for cryogenic calorimeters, J. Low. Temp. Phys. **167**, 485 (2012).

[24] S. W. Leman, K. A. McCarthy, P. L. Brink, B. Cabrera, M. Cherry, E. S. E. Do Couto, E. Figueroa-Feliciano, P. Kim, N. Mirabolfathi, M. Pyle, R. Resch, B. Sadoulet, B. Serfass, K. M. Sundqvist, A. Tomada, and B. A. Young, Monte carlo comparisons to a cryogenic dark matter search detector with low transition-edge-Sensor transition temperature, J. Appl. Phys. **110**, 094515 (2011).

[25] K. A. McCarthy, S. W. Leman, A. Anderson, D. Brandt, P. L. Brink, B. Cabrera, M. Cherry, E. Do Couto E Silva, P. Cushman, T. Doughty, E. Figueroa-Feliciano, P. Kim, N. Mirabolfathi, L. Novak, and R. Partridge, *et al.*, Validation of phonon physics in the CDMS detector monte carlo, J. Low. Temp. Phys. **167**, 1160 (2012).

[26] E. T. Swartz and R. O. Pohl, Thermal boundary resistance, Rev. Mod. Phys. **61**, 605 (1989).

[27] E. T. Swartz and R. O. Pohl, Thermal resistance at interfaces, App. Phys. Lett. **51**, 2200 (1987).

[28] C. Hua, X. Chen, N. K. Ravichandran, and A. J. Minnich, Experimental Metrology to Obtain Thermal Phonon Transmission Coefficients at Solid Interfaces, Phys. Rev. B **95**, 205423 (2017).

[29] E. S. Battistelli, F. Bellini, C. Bucci, M. Calvo, L. Cardani, N. Casali, M. G. Castellano, I. Colantoni, A. Coppolecchia, C. Cosmelli, A. Cruciani, P. de Bernardis, S. Di Domizio, A. D'Addabbo, M. Martinez, S. Masi, L. Pagnanini, C. Tomei, and M. Vignati, CALDER – neutrinoless double-beta decay identification in TeO_2 bolometers with kinetic inductance detectors, Eur. Phys. J. **C75**, 353 (2015).

[30] S. W. Leman, Review article: Physics and monte carlo techniques as relevant to cryogenic, phonon and ionization readout of CDMS radiation-detectors, Rev. Sci. Instrum. **83**, 091101 (2012).

[31] S.-I. Tamura, Spontaneous decay rates of LA phonons in quasi-isotropic solids, Phys. Rev. B **31**, 2574 (1985).

[32] N. W. Ashcroft and N. D. Mermin, *Solid State Physics* (Harcourt, Orlando, 1976).

[33] S. Tamura, J. A. Shields, and J. P. Wolfe, Lattice dynamics and elastic phonon scattering in silicon, Phys. Rev. B **44**, 3001 (1991).

[34] S.-I. Tamura, Quasidiffusive propagation of phonons in silicon: Monte carlo calculations, Phys. Rev. B **48**, 13502 (1993).

[35] A. G. Kozorezov, A. F. Volkov, J. K. Wigmore, A. Peacock, A. Poelaert, and R. den Hartog, Quasiparticle-phonon downconversion in nonequilibrium superconductors, Phys. Rev. B **61**, 11807 (2000).

[36] B. Taylor, H. J. Maris, and C. Elbaum, Phonon Focusing in Solids, Phys. Rev. Lett. **23**, 416 (1969).

[37] G. A. Northrop and J. P. Wolfe, Ballistic Phonon Imaging in Solids-A New Look at Phonon Focusing, Phys. Rev. Lett. **43**, 1424 (1979).

[38] D. C. Hurley and J. P. Wolfe, Phonon focusing in cubic crystals, Phys. Rev. B **32**, 2568 (1985).

[39] J. P. Wolfe, *Imaging Phonons* (Cambridge University Press, Cambridge, 2005).

[40] S. Doyle, P. Mauskopf, J. Naylon, A. Porch, and C. Duncombe, Lumped element kinetic inductance detectors, J. Low Temp. Phys. **151**, 530 (2008).

[41] I. Colantoni, F. Bellini, L. Cardani, N. Casali, M. G. Castellano, A. Coppolecchia, C. Cosmelli, A. Cruciani, A. D'Addabbo, S. Di Domizio, M. Martinez, C. Tomei, and M. Vignati, Fabrication of the CALDER light detectors, Nucl. Instrum. Methods Phys. Res. A **824**, 177 (2016).

[42] I. Colantoni, F. Bellini, L. Cardani, N. Casali, M. G. Castellano, A. Coppolecchia, C. Cosmelli, A. Cruciani, A. D'Addabbo, S. Di Domizio, M. Martinez, C. Tomei, and M. Vignati, Design and fabrication of the KID-based light detectors of CALDER, J. Low. Temp. Phys. **184**, 131 (2016).

[43] N. Casali, F. Bellini, L. Cardani, M. G. Castellano, I. Colantoni, A. Coppolecchia, C. Cosmelli, A. Cruciani, A. D'Addabbo, S. Di Domizio, M. Martinez, C. Tomei, and M. Vignati, Characterization of the KID-based light detectors of CALDER, J. Low. Temp. Phys. **184**, 142 (2016).

[44] L. Cardani, N. Casali, I. Colantoni, A. Cruciani, F. Bellini, M. G. Castellano, C. Cosmelli, A. D'Addabbo, S. Di Domizio, M. Martinez, C. Tomei, and M. Vignati, High sensitivity phonon-mediated kinetic inductance detector with combined amplitude and phase read-out, Appl. Phys. Lett. **110**, 033504 (2017).

[45] P. J. de Visser, D. J. Goldie, P. Diener, S. Withington, J. J. A. Baselmans, and T. M. Klapwijk, Evidence of a Nonequilibrium Distribution of Quasiparticles in the Microwave Response of a Superconducting Aluminum Resonator, Phys. Rev. Lett. **112**, 047004 (2014).

[46] B. A. Mazin, Ph.D. thesis, Caltech (2004).

[47] J. Gao, J. Zmuidzinas, B. A. Mazin, P. K. Day, and H. G. Leduc, Experimental study of the kinetic inductance fraction of superconducting coplanar waveguide, Nucl. Instr. Meth. **559**, 585 (2006).

[48] L. Cardani, N. Casali, A. Cruciani, H. le Sueur, M. Martinez, F. Bellini, M. Calvo, M. G. Castellano, I. Colantoni, C. Cosmelli, A. D'Addabbo, S. Di Domizio, J. Goupy, L. Minutolo, and M. Vignat Al/Ti/Al phonon-mediated KIDs for UV-vis light detection over large areas, Supercond. Sci. Technol. **31**, 075002 (2018).

[49] H. J. McSkimin and P. Andreatch, Jr., Measurement of third-order moduli of silicon and germanium, J. App. Phys. **35**, 3312 (1964).

[50] O. H. Nielsen and R. M. Martin, Stresses in semiconductors: Ab initio calculations on Si, Ge, and GaAs, Phys. Rev. B **32**, 3792 (1985).

[51] A.-B. Chen, A. Sher, and W. Yost, in *The Mechanical Properties of Semiconductors*, edited by K. T. Faber and K. J. Malloy (Elsevier, 1992), vol. 37 of *Semiconductors and Semimetals*, p. 1.

[52] G. A. Northrop and J. P. Wolfe, Phonon Reflection Imaging: A Determination of Specular versus Diffuse Boundary Scattering, Phys. Rev. Lett. **52**, 2156 (1984).